

Low-loss interconnects for modular superconducting quantum processors

Received: 23 May 2022

Accepted: 17 January 2023

Published online: 16 February 2023



Jingjing Niu^{1,2,3,4}, Libo Zhang^{1,2,3}, Yang Liu^{1,2,3}, Jiawei Qiu^{1,2,3}, Wenhui Huang^{1,2,3}, Jiaxiang Huang^{1,2,3}, Hao Jia^{1,2,3}, Jiawei Liu^{1,2,3}, Ziyu Tao^{1,2,3}, Weiwei Wei^{1,2,3}, Yuxuan Zhou^{1,2,3}, Wanjin Zou^{1,2,3}, Yuanzhen Chen^{1,2,3,5}, Xiaowei Deng^{1,2,3}, Xiu hao Deng^{1,2,3}, Changkang Hu^{1,2,3}, Ling Hu^{1,2,3}, Jian Li^{1,2,3}, Dian Tan^{1,2,3}, Yuan Xu^{1,2,3,4}, Fei Yan^{1,2,3}, Tongxing Yan^{1,2,3}, Song Liu^{1,2,3,4}✉, Youpeng Zhong^{1,2,3,4}✉, Andrew N. Cleland^{6,7} & Dapeng Yu^{1,2,3,4,5}

Scaling is now a key challenge in superconducting quantum computing. One solution is to build modular systems in which smaller-scale quantum modules are individually constructed and calibrated and then assembled into a larger architecture. This, however, requires the development of suitable interconnects. Here we report low-loss interconnects based on pure aluminium coaxial cables and on-chip impedance transformers featuring quality factors of up to 8.1×10^5 , which is comparable with the performance of our transmon qubits fabricated on a single-crystal sapphire substrate. We use these interconnects to link five quantum modules with intermodule quantum state transfer and Bell state fidelities of up to 99%. To benchmark the overall performance of the processor, we create maximally entangled, multiqubit Greenberger–Horne–Zeilinger states. The generated intermodule four-qubit Greenberger–Horne–Zeilinger state exhibits 92.0% fidelity. We also entangle up to 12 qubits in a Greenberger–Horne–Zeilinger state with $55.8 \pm 1.8\%$ fidelity, which is above the genuine multipartite entanglement threshold of $1/2$.

Superconducting quantum circuits could be used to build scalable quantum processors¹. The size of such circuits has increased over the past decade, from a handful of qubits to over a hundred qubits^{2–4}. However, the near-term development of processors with thousands of qubits⁴ for use in intermediate-scale applications⁵ comes with a range of engineering challenges—including available wafer size, device yield and crosstalk^{6,7}—that limit the development of monolithic quantum processors. An alternative approach is to build modular systems^{7–12}, where smaller-scale quantum modules are individually constructed and calibrated and then assembled into a larger architecture using quantum coherent interconnects. Similar strategies have been pursued

in other quantum systems, including those using atoms^{13,14}, ions¹⁰ and spin-based qubits¹⁵. Modular quantum computing schemes may be the most viable approach to scaling up to very large qubit numbers in the near term⁷. However, high-quality interconnects that can transfer vulnerable quantum states between separate processors are needed^{7,9}.

Reaching the fundamental loss limit for waveguides transmitting signals has been key to the development of our information society. For example, with a loss of only 0.2 dB km^{-1} , optical fibres form the basis of global telecommunication networks. The pursuit of low-loss transmission is also important in radio-frequency cables. With the development of quantum information science, the need for low-loss

¹Shenzhen Institute for Quantum Science and Engineering, Southern University of Science and Technology, Shenzhen, China. ²International Quantum Academy, Shenzhen, China. ³Guangdong Provincial Key Laboratory of Quantum Science and Engineering, Southern University of Science and Technology, Shenzhen, China. ⁴Shenzhen Branch, Hefei National Laboratory, Shenzhen, China. ⁵Department of Physics, Southern University of Science and Technology, Shenzhen, China. ⁶Pritzker School of Molecular Engineering, University of Chicago, Chicago, IL, USA. ⁷Center for Molecular Engineering and Material Science Division, Argonne National Laboratory, Argonne, IL, USA. ✉e-mail: lius3@sustech.edu.cn; zhongyp@sustech.edu.cn

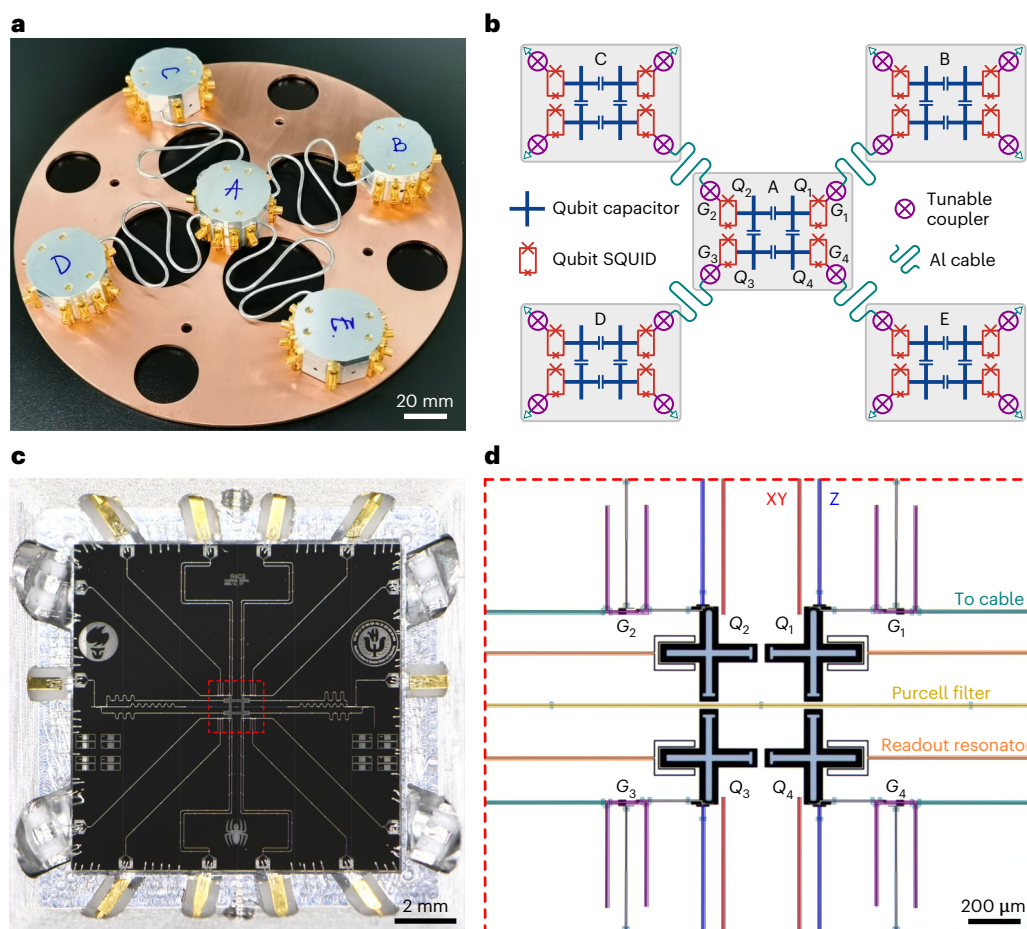


Fig. 1 | Modular quantum processor design. **a**, Photograph of the modular quantum processor assembly. **b**, Schematic of the circuit of the modular processor. The blue crosses represent the qubit capacitor pads; the red rectangles with crosses represent the qubit junction loops (with asymmetric junction sizes); the purple circles represent tunable couplers, where the cross

inside represents a Josephson junction; the serpentine cyan lines represent the Al cables. The unused couplers are shorted to ground by bonding wires. SQUID, superconducting quantum interference device. **c**, Photograph of central module A, showing a spider-shaped circuit layout. **d**, Detailed micrograph of module A (as shown in **c**), showing the qubits, tunable couplers and control/readout circuitry.

cables/waveguides has become imperative⁷. Several recent experiments have demonstrated the connection of two superconducting quantum modules using niobium–titanium (NbTi) superconducting coaxial cables^{6,16–21}. Intermodule quantum-state-transfer (QST) fidelities of up to 91.1% have been reached, but this is still not sufficient for large-scale system deployment.

Flip-chip schemes have also been investigated^{22–24}, achieving high fidelities and retaining many benefits of a modular architecture. The routinely used NbTi cables have a linear loss of ~ 5 dB km^{−1}, corresponding to a cable intrinsic quality factor (Q_{cb}) of $\sim 10^5$ (refs. ^{6,16–18,21}). In contrast to NbTi cables that have already been commercialized, pure aluminium (Al) cables could be used. However, they are not readily available, partially due to the low superconducting transition temperature (T_c) of Al. In this Article, we report coherent interconnects using low-loss coaxial cables made from pure Al, with Al wire-bonded connections to qubit processors. Although $T_c = 1.2$ K of Al is much lower than that of NbTi (9.7 K), the Q_{cb} value of our cables at ~ 10 mK reaches 4.2×10^6 , which is equivalent to a loss of 0.15 dB km^{−1}.

Modular quantum system architecture

Our modular quantum processor consists of five modules (Fig. 1), where each module n ($n = \text{A–E}$) has four capacitively coupled transmon qubits Q_i^n ($i = 1–4$), each qubit galvanically connected to a tunable coupler²⁵ G_i^n for external connections. The five quantum modules are first

individually calibrated at cryogenic temperatures to confirm that all the components function properly. We then mount them on a circular copper plate and use four 0.25-m-long Al cables cut from a 1.00-m-long cable to link the modules together in the star topology, where A is the central module and B–E are on the periphery (Fig. 1a,b). To reduce the cable counts, each qubit's XY and Z control lines are combined using diplexers. To suppress dephasing noise and retain some frequency tunability, we use asymmetric Josephson junctions with $\alpha = E_{J1}/E_{J2} = 5.3$, where E_{J1} and E_{J2} are the Josephson energies of the two qubit junctions, giving a qubit frequency-tuning range of ~ 4.2 to ~ 5.1 GHz. More experimental details can be found in Supplementary Section II.

We first tune up and characterize the interconnects. When the tunable couplers are tuned off, the coaxial cable is effectively shorted to ground by the tunable couplers at each end²¹, supporting an evenly spaced sequence of standing microwave modes, with a free spectral range $\omega_{\text{FSR}}/2\pi \approx 0.44$ GHz determined by the cable length (Fig. 2a). We now focus on the interconnect between modules A and B. When we prepare qubit Q_1^A in its excited state $|1\rangle$ and subsequently turn on the coupler G_1^A , we observe vacuum Rabi oscillations between Q_1^A and the cable standing-wave modes when the qubit frequency matches with the m th-mode frequency of $\omega_m/2\pi$ (ref. ²¹) (Fig. 2b). The qubit frequency-tuning range here allows access to the $m = 10$ mode at 4.450 GHz and the $m = 11$ mode at 4.885 GHz. The ~ 6.5 -mm-long on-chip coplanar waveguide (CPW) line is essentially a quarter-wavelength

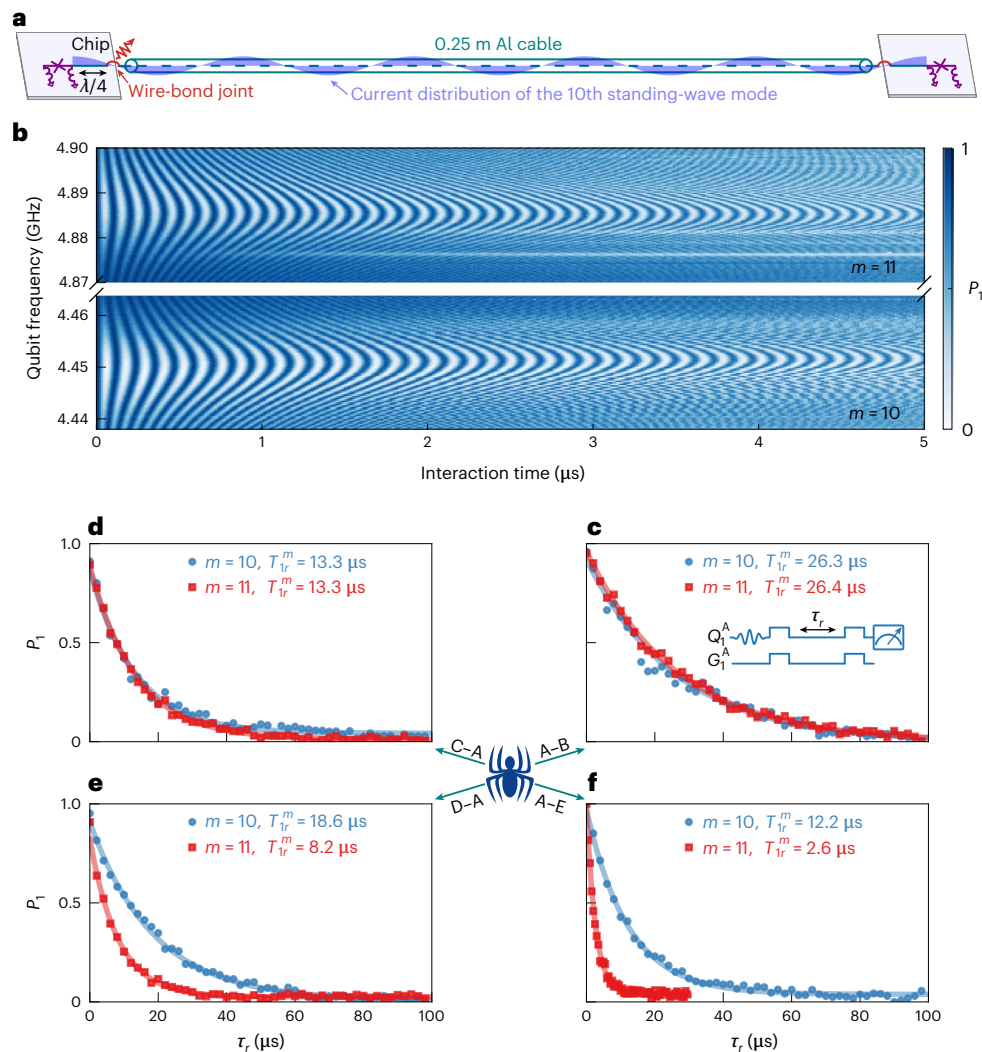


Fig. 2 | Characterization of superconducting Al cable interconnects. a, Schematic of the chip–cable–chip interconnect (cyan), shorted to ground at both ends by tunable couplers (purple). The current distribution of the 10th standing-wave mode is depicted (light blue). The on-chip CPW $\lambda/4$ impedance transformer is designed to match the 10th standing-wave mode such that the wire-bond joint (red) coincides with a current node, thus minimizing the current-induced dissipation at the wire-bond joint (Supplementary Fig. 1). We use Q_1^A to measure the lifetime T_{lr}^m of the two modes by first swapping a photon from Q_1^A to the mode, waiting for time τ_r and then swapping out the photon. The population P_1 of the qubit excited state $|1\rangle$ is then measured and it exponentially decays with time constant T_{lr}^m (Fig. 2c). Fitting the data gives $T_{lr}^m = 26.3 \mu\text{s}$ for the 10th mode and $26.4 \mu\text{s}$ for the 11th mode, comparable with the native coherence of the transmon qubits. Other interconnects are characterized in the same way (Fig. 2d–f), where the performance is somewhat non-uniform. The best performance is found for the 11th mode in the A–B interconnect, with a standing-mode internal quality factor of $Q_{\text{int}}^m = \omega_m T_{lr}^m = 8.1 \times 10^5$. In comparison, state-of-the-art coplanar waveguides fabricated using ultrahigh-vacuum molecular-beam epitaxy deposited Al on a single-crystal sapphire substrate have achieved a quality factor of merely above 10^6 at single-photon levels²⁶.

between Q_1^A and the $m=10$ and $m=11$ standing-wave modes in the A–B interconnect. **c–f**, Lifetime T_{lr}^m of the $m=10$ and $m=11$ standing-wave modes in the four interconnects, measured using their associated qubits in module A. The 11th mode in the A–B interconnect has the highest internal quality factor of $Q_{\text{int}}^m = \omega_m T_{lr}^m = 8.1 \times 10^5$. The inset in **c** shows the control-pulse sequence for lifetime measurement. The spider symbol represents the central module A.

($\lambda/4$) impedance transformer designed to match the 10th standing-wave mode, such that the wire-bond joint coincides with a current node (Fig. 2a), thus minimizing the current-induced dissipation at the wire-bond joint (Supplementary Fig. 1). We use Q_1^A to measure the lifetime T_{lr}^m of the two modes by first swapping a photon from Q_1^A to the mode, waiting for time τ_r and then swapping out the photon. The population P_1 of the qubit excited state $|1\rangle$ is then measured and it exponentially decays with time constant T_{lr}^m (Fig. 2c). Fitting the data gives $T_{lr}^m = 26.3 \mu\text{s}$ for the 10th mode and $26.4 \mu\text{s}$ for the 11th mode, comparable with the native coherence of the transmon qubits. Other interconnects are characterized in the same way (Fig. 2d–f), where the performance is somewhat non-uniform. The best performance is found for the 11th mode in the A–B interconnect, with a standing-mode internal quality factor of $Q_{\text{int}}^m = \omega_m T_{lr}^m = 8.1 \times 10^5$. In comparison, state-of-the-art coplanar waveguides fabricated using ultrahigh-vacuum molecular-beam epitaxy deposited Al on a single-crystal sapphire substrate have achieved a quality factor of merely above 10^6 at single-photon levels²⁶.

Following another work²¹, we use a hybrid scheme to transfer quantum states between modules A and B using the 11th standing-wave mode R and both ‘dark’ and ‘bright’ eigenmodes of the Q_1^A – R – Q_3^B tripartite system. This scheme balances the loss in the communication mode as well as in the qubits²⁷. We bias the couplers G_1^A and G_3^B to set the Q_1^A – R coupling g_1^A and the Q_3^B – R coupling g_3^B to the same strength of $g_0/2\pi = 5 \text{ MHz}$, as well as tuning both Q_1^A and Q_3^B to resonantly interact with R for duration τ (Fig. 3a). We note that although stronger coupling can be achieved here, extrinsic qubit loss could emerge as the coupling increases, exposing the qubits to loss channels at the wire-bond joint²¹. The coupling strength g_0 chosen here is similar to that in the other work²¹, which balances intrinsic decoherence with extrinsic loss. At $\tau = 66 \text{ ns}$, one photon is transferred from Q_1^A to Q_3^B with optimal fidelity. We perform quantum process tomography (Supplementary Section V) to characterize this QST process, yielding the process matrix χ (Fig. 3b) with a fidelity of $\mathcal{F}_{\text{QST}} = \text{Tr}(\chi\chi_{\mathcal{I}}) = 99.1 \pm 0.5\%$, where $\chi_{\mathcal{I}}$ is the process matrix for the identity operation \mathcal{I} . Note that all the uncertainties reported here represent the standard deviation of repeated

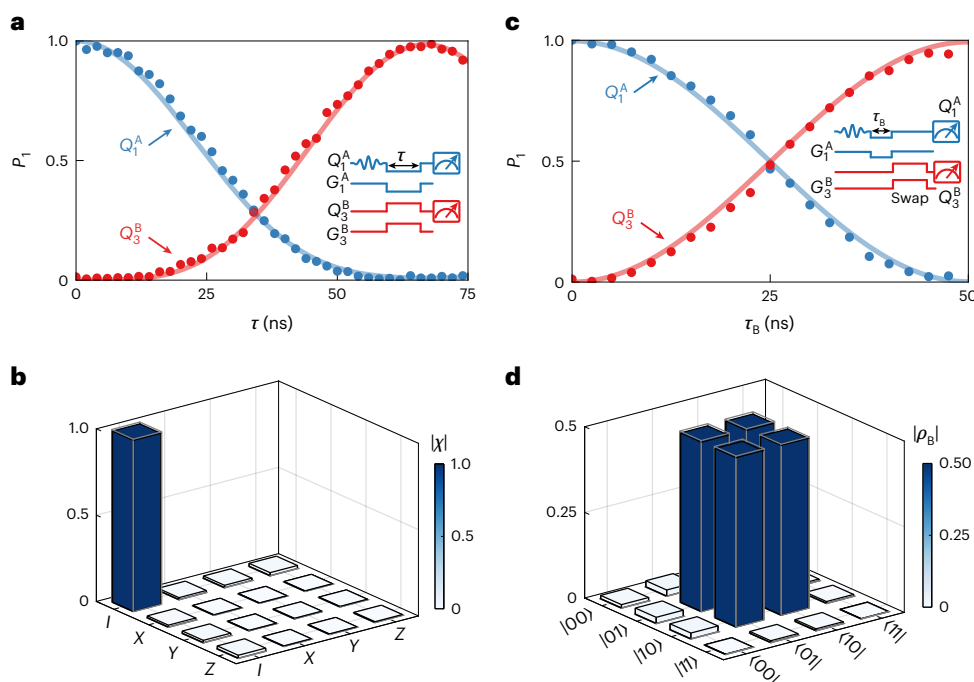


Fig. 3 | High-fidelity intermodule QST and entanglement generation. a, Transferring a photon from Q_1^A to Q_3^B . **b**, Quantum process tomography of the state transfer shown in **a** at $\tau = 66$ ns, with a process fidelity of $\mathcal{F}_{\text{QST}} = 99.1 \pm 0.5\%$. The horizontal axes are the Pauli operators I, X, Y and Z . **c**, Intermodule

entanglement generation. **d**, Density matrix of the Bell state generated in **c** at $\tau_B = 25$ ns with a state fidelity of $\mathcal{F}_B = 98.9 \pm 0.6\%$. In **a** and **c**, the lines are simulations and the insets are control-pulse sequences; in **b** and **d**, the solid bars and grey frames are the measured and ideal values, respectively.

measurements. Numerical simulations give a process fidelity of $\mathcal{F}_{\text{QST}} = 99.3\%$, agreeing well with the experiment. A numerical analysis suggests that this fidelity is mainly limited by qubit decoherence; further improvement in QST fidelity requires a faster QST process and/or longer qubit coherence time. In addition to transferring quantum states, we can also generate entanglement across modules, such as by preparing a Bell singlet state $|\psi_B\rangle = (|01\rangle + |10\rangle)/\sqrt{2}$ (here $|0\rangle$ is the qubit ground state) using a half-photon swap. We first turn on the Q_1^A – R interaction for $\tau_B = 25$ ns, sharing half a photon with R and then swapping this entangled photon from R to Q_3^B (ref. ²⁸), a process we denote as QST/2 (Fig. 3c). The density matrix ρ_B of the resulting Bell state, obtained from quantum state tomography (Supplementary Section V), is shown in Fig. 3d, with a state fidelity of $\mathcal{F}_B = \langle\psi_B|\rho_B|\psi_B\rangle = 98.9 \pm 0.6\%$, where numerical simulations give a very similar fidelity of $\mathcal{F}_B = 99.1\%$. The other interconnects give similar results, with an average QST fidelity of 98.2% and Bell state fidelity of 98.6% (Supplementary Table 3).

Benchmarking the modular processor performance

With the qubits and interconnects carefully tuned up, we now benchmark the modular processor as a whole. Greenberger–Horne–Zeilinger (GHZ) states²⁹ are a fundamental resource in fault-tolerant quantum computation and quantum communication; as they are highly susceptible to errors and decoherence, they provide a sensitive benchmark for our processor. We use controlled-NOT (CNOT) gates to generate GHZ states in a step-by-step manner by following the protocol shown in Fig. 4a, eventually entangling up to 12 qubits. The CNOT gates are composed of fast adiabatic controlled-Z (CZ) gates³⁰ and single-qubit rotations, where the single-qubit gates have an average fidelity of 99.85% and the CZ gates have an average fidelity of 96.10% (Supplementary Fig. 8). Starting from the Bell state (Fig. 3d), we simultaneously apply CNOT gates on both sides to first generate a four-qubit GHZ

state between modules A and B, yielding $|\psi_4\rangle = (|0\rangle^{\otimes 4} + |1\rangle^{\otimes 4})/\sqrt{2}$. The measured density matrix ρ_4 of this state is shown in Fig. 4b, with a fidelity of $\mathcal{F}_4 = \langle\psi_4|\rho_4|\psi_4\rangle = 92.0 \pm 0.6\%$. We note that this state fidelity rivals its state-of-the-art monolithic counterparts^{30–33}, highlighting the capability and potential of the low-loss interconnects. We then perform two more CNOT gates in parallel, yielding a six-qubit GHZ state of $|\psi_6\rangle = (|0\rangle^{\otimes 6} + |1\rangle^{\otimes 6})/\sqrt{2}$ (Fig. 4c) with a fidelity of $\mathcal{F}_6 = 83.2 \pm 0.8\%$. To further expand the entanglement, we distribute the GHZ state to module E using the 10th mode and apply more CNOT gates, eventually yielding a 10-qubit (step (iii)) and 12-qubit (step (iv)) GHZ state, where module E is chosen because of its higher-performance interconnect (Supplementary Table 3). As quantum state tomography requires measurements and computational resources that grow exponentially with the number of qubits, a full characterization of these two states is impractical³⁴. Nevertheless, the density matrix ρ of an ideal N -qubit GHZ state has only four non-zero elements: two diagonal elements $\rho_{0\dots 0,0\dots 0}$ and $\rho_{1\dots 1,1\dots 1}$, and two conjugate off-diagonal elements $\rho_{0\dots 0,1\dots 1}$ and $\rho_{1\dots 1,0\dots 0}$, allowing one to evaluate the state fidelity in an easier way. The diagonal elements are simply the qubit joint-readout probabilities $P_{0\dots 0}$ and $P_{1\dots 1}$. To access the off-diagonal terms, we measure the expectation value of the operator $\mathcal{P}(\gamma) = \otimes_{q=1}^N (\cos\gamma X_q + \sin\gamma Y_q)$ (ref. ³⁴), where q is the qubit index; X_q and Y_q are the Pauli operators for qubit q ; and $\gamma \in [0, 2\pi]$. Ideally, $\langle\mathcal{P}(\gamma)\rangle = 2|\rho_{1\dots 1,0\dots 0}| \cos(N\gamma + \phi_0)$, where ϕ_0 is the phase of $\rho_{1\dots 1,0\dots 0}$. The oscillation period of $2\pi/N$ is a unique feature of the N -qubit GHZ state. The GHZ state fidelity is then given by $\mathcal{F}_N = (P_{0\dots 0} + P_{1\dots 1} + 2|\rho_{1\dots 1,0\dots 0}|)/2$. In Fig. 4d,e, we show the measured $\langle\mathcal{P}(\gamma)\rangle$ for the 10-qubit and 12-qubit GHZ states, respectively. Combining these measurements with the qubit joint-readout probabilities, we estimate the GHZ state fidelities as $\mathcal{F}_{10} = 63.0 \pm 1.5\%$ and $\mathcal{F}_{12} = 55.8 \pm 1.8\%$, respectively, clearly above the threshold of $1/2$ for genuine multipartite entanglement³⁵. To our knowledge, this represents the largest quantum entanglement generated in solid-state systems separated by a macroscopic distance to date. We are not

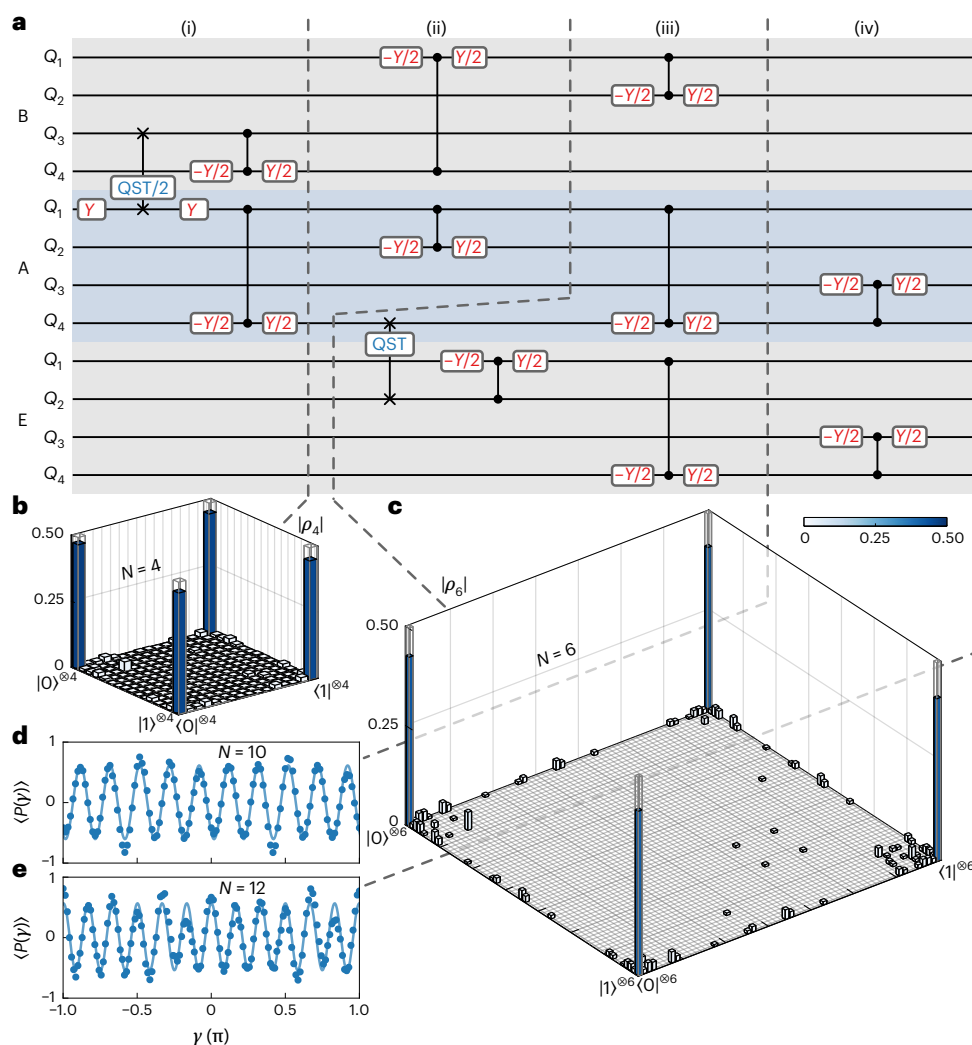


Fig. 4 | Performance benchmarking using entanglement generation. a, Protocol for GHZ state generation. In step (iii), the QST from module A to E is moved forward to shorten the sequence length. **b,** Four-qubit GHZ state density matrix ρ_4 generated in step (i) with a fidelity of $\mathcal{F}_4 = 92.0 \pm 0.6\%$. **c,** Six-qubit GHZ state density matrix ρ_6 generated in step (ii), with a fidelity of $\mathcal{F}_6 = 83.2 \pm 0.8\%$. For simplicity, density matrix elements smaller than 0.005 are not displayed. **d,e,**

Measured $\langle \mathcal{P}(\gamma) \rangle$ oscillation for the $N=10$ and $N=12$ GHZ states generated in steps (iii) and (iv), respectively. From the oscillation amplitude and qubit joint-readout probabilities, we estimate the corresponding GHZ state fidelity as $\mathcal{F}_{10} = 63.0 \pm 1.5\%$ and $\mathcal{F}_{12} = 55.8 \pm 1.8\%$, respectively. The solid bars and grey frames in **b** and **c** are the measured and ideal values, respectively.

able to entangle all the qubits on this modular processor with a meaningful fidelity, mainly limited by qubit decoherence and CZ gate error.

Conclusions

We have reported low-loss quantum interconnects that reach the native coherence of superconducting qubits. With linear losses as low as optical fibres, these cables could be used in a range of microwave applications at cryogenic temperatures, including modular quantum computing, quantum networks⁹, quantum optics³⁶, quantum non-locality tests³⁷, hybrid quantum systems³⁸, microwave delay lines³⁹ and radio astronomy. Here we have demonstrated their use in linking together quantum modules to create a large-scale quantum computing system. We have shown high-fidelity intermodule QST, entanglement generation and large-scale entangled states linking multiple quantum modules, rivalling those of monolithic designs. Our approach could be used to scale up modular superconducting quantum processors to large sizes and explore sophisticated quantum computation and simulation tasks.

Data availability

The data that support the plots within this paper and other findings of this study are available from the corresponding authors upon reasonable request.

References

1. Kjaergaard, M. et al. Superconducting qubits: current state of play. *Annu. Rev. Condens. Matter Phys.* **11**, 369–395 (2020).
2. Arute, F. et al. Quantum supremacy using a programmable superconducting processor. *Nature* **574**, 505–510 (2019).
3. Wu, Y. et al. Strong quantum computational advantage using a superconducting quantum processor. *Phys. Rev. Lett.* **127**, 180501 (2021).
4. Ball, P. First quantum computer to pack 100 qubits enters crowded race. *Nature* **599**, 542 (2021).
5. Preskill, J. Quantum computing in the NISQ era and beyond. *Quantum* **2**, 79 (2018).

6. Burkhardt, L. D. et al. Error-detected state transfer and entanglement in a superconducting quantum network. *PRX Quantum* **2**, 030321 (2021).
7. Awschalom, D. et al. Development of quantum interconnects (QulCs) for next-generation information technologies. *PRX Quantum* **2**, 017002 (2021).
8. Jiang, L., Taylor, J. M., Sørensen, A. S. & Lukin, M. D. Distributed quantum computation based on small quantum registers. *Phys. Rev. A* **76**, 062323 (2007).
9. Kimble, H. J. The quantum internet. *Nature* **453**, 1023–1030 (2008).
10. Monroe, C. et al. Large-scale modular quantum-computer architecture with atomic memory and photonic interconnects. *Phys. Rev. A* **89**, 022317 (2014).
11. Chou, K. S. et al. Deterministic teleportation of a quantum gate between two logical qubits. *Nature* **561**, 368–373 (2018).
12. LaRacune, N., Smith, K. N., Imany, P., Silverman, K. L. & Chong, F. T. Modeling short-range microwave networks to scale superconducting quantum computation. Preprint at *arXiv* <https://arxiv.org/abs/2201.08825v2> (2023).
13. Ritter, S. et al. An elementary quantum network of single atoms in optical cavities. *Nature* **484**, 195–200 (2012).
14. Dordevic, T. et al. Entanglement transport and a nanophotonic interface for atoms in optical tweezers. *Science* **373**, 1511–1514 (2021).
15. Pompili, M. et al. Realization of a multinode quantum network of remote solid-state qubits. *Science* **372**, 259–264 (2021).
16. Kurpiers, P. et al. Deterministic quantum state transfer and remote entanglement using microwave photons. *Nature* **558**, 264–267 (2018).
17. Axline, C. J. et al. On-demand quantum state transfer and entanglement between remote microwave cavity memories. *Nat. Phys.* **14**, 705–710 (2018).
18. Campagne-Ibarcq, P. et al. Deterministic remote entanglement of superconducting circuits through microwave twophoton transitions. *Phys. Rev. Lett.* **120**, 200501 (2018).
19. Leung, N. et al. Deterministic bidirectional communication and remote entanglement generation between superconducting qubits. *Quantum Inf.* **5**, 18 (2019).
20. Magnard, P. et al. Microwave quantum link between superconducting circuits housed in spatially separated cryogenic systems. *Phys. Rev. Lett.* **125**, 260502 (2020).
21. Zhong, Y. et al. Deterministic multi-qubit entanglement in a quantum network. *Nature* **590**, 571–575 (2021).
22. Gold, A. et al. Entanglement across separate silicon dies in a modular superconducting qubit device. *Quantum Inf.* **7**, 142 (2021).
23. Conner, C. R. et al. Superconducting qubits in a flip-chip architecture. *Appl. Phys. Lett.* **118**, 232602 (2021).
24. Kosen, S. et al. Building blocks of a flip-chip integrated superconducting quantum processor. *Quantum Sci. Technol.* **7**, 035018 (2022).
25. Chen, Y. et al. Qubit architecture with high coherence and fast tunable coupling. *Phys. Rev. Lett.* **113**, 220502 (2014).
26. Megrant, A. et al. Planar superconducting resonators with internal quality factors above one million. *Appl. Phys. Lett.* **100**, 113510 (2012).
27. Wang, Y.-D. & Clerk, A. A. Using dark modes for high-fidelity optomechanical quantum state transfer. *New J. Phys.* **14**, 105010 (2012).
28. Zhong, Y. P. et al. Violating Bell's inequality with remotely connected superconducting qubits. *Nat. Phys.* **15**, 741–744 (2019).
29. Greenberger, D. M., Horne, M. A., Shimony, A. & Zeilinger, A. Bell's theorem without inequalities. *Am. J. Phys.* **58**, 1131–1143 (1990).
30. Barends, R. et al. Superconducting quantum circuits at the surface code threshold for fault tolerance. *Nature* **508**, 500–503 (2014).
31. Song, C. et al. 10-qubit entanglement and parallel logic operations with a superconducting circuit. *Phys. Rev. Lett.* **119**, 180511 (2017).
32. Wei, K. X. et al. Verifying multipartite entangled Greenberger-Horne-Zeilinger states via multiple quantum coherences. *Phys. Rev. A* **101**, 032343 (2020).
33. Marques, J. F. et al. Logical-qubit operations in an error-detecting surface code. *Nat. Phys.* **16**, 875–880 (2021).
34. Song, C. et al. Generation of multicomponent atomic Schrödinger cat states of up to 20 qubits. *Science* **365**, 574–577 (2019).
35. Gühne, O. & Seevinck, M. Separability criteria for genuine multipartite entanglement. *New J. Phys.* **12**, 053002 (2010).
36. Blais, A., Girvin, S. M. & Oliver, W. D. Quantum information processing and quantum optics with circuit quantum electrodynamics. *Nat. Phys.* **16**, 247–256 (2020).
37. Hensen, B. et al. Loophole-free Bell inequality violation using electron spins separated by 1.3 kilometres. *Nature* **526**, 682–686 (2015).
38. Tabuchi, Y. et al. Coherent coupling between a ferromagnetic magnon and a superconducting qubit. *Science* **349**, 405–408 (2015).
39. Su, H. T., Wang, Y., Huang, F. & Lancaster, M. J. Superconducting delay lines. *J. Supercond. Nov. Magn.* **21**, 7–16 (2008).

Acknowledgements

We thank Y. He and J. Liu for helpful discussions and critical reading of the manuscript. This work was supported by the Key Area Research and Development Program of Guangdong Province (2018B030326001); the National Natural Science Foundation of China (U1801661, 12174178); the Guangdong Innovative and Entrepreneurial Research Team Program (2016ZT06D348); the Guangdong Provincial Key Laboratory (2019B121203002); the Science, Technology and Innovation Commission of Shenzhen Municipality (KYTDPT20181011104202253, KQTD20210811090049034); the Shenzhen-Hong Kong Cooperation Zone for Technology and Innovation (HZQB-KCZYB-2020050); and the NSF of Beijing (Z190012) and the Innovation Program for Quantum Science and Technology (2021ZD0301703).

Author contributions

Y. Zhong conceived the idea and supervised the experiment. S.L. supervised the device fabrication and supported the infrastructure setup. J.N. and Y. Zhong wire-bonded the cables, performed the measurement and analysed the data. L.Z. fabricated the devices and designed the sample holder. Y.L. and J.Q. assisted in the measurement. Y. Zhong built the custom microwave electronics. Y. Zhong and A.N.C. wrote the manuscript. All the authors contributed to the discussions and production of the manuscript.

Competing interests

Y. Zhong, S.L., D.Y., J.N. and L.Z. are inventors on a provisional patent application (China, 202210723073.8) that has been filed relating to this work. The other authors declare no competing interests.

Additional information

Supplementary information The online version contains supplementary material available at <https://doi.org/10.1038/s41928-023-00925-z>.

Correspondence and requests for materials should be addressed to Song Liu or Youpeng Zhong.

Peer review information *Nature Electronics* thanks the anonymous reviewers for their contribution to the peer review of this work.

Reprints and permissions information is available at www.nature.com/reprints.

Publisher's note Springer Nature remains neutral with regard to jurisdictional claims in published maps and institutional affiliations.

Springer Nature or its licensor (e.g. a society or other partner) holds exclusive rights to this article under a publishing agreement with the author(s) or other rightsholder(s); author self-archiving of the accepted manuscript version of this article is solely governed by the terms of such publishing agreement and applicable law.

© The Author(s), under exclusive licence to Springer Nature Limited 2023